



Cite this: DOI: 10.1039/c5nr09087c

Received 21st December 2015,
 Accepted 5th February 2016

DOI: 10.1039/c5nr09087c

www.rsc.org/nanoscale

A three-dimensional integrated nanogenerator for effectively harvesting sound energy from the environment†

Jinmei Liu,^{‡a} Nuanyang Cui,^{‡a} Long Gu,^a Xiaobo Chen,^a Suo Bai,^{a,b} Youbin Zheng,^a Caixia Hu^a and Yong Qin^{*a,b}

An integrated triboelectric nanogenerator (ITNG) with a three-dimensional structure benefiting sound propagation and adsorption is demonstrated to more effectively harvest sound energy with improved output performance. With different multifunctional integrated layers working harmonically, it could generate a short-circuit current up to 2.1 mA, an open-circuit voltage up to 232 V and the maximum charging rate can reach 453 $\mu\text{C s}^{-1}$ for a 1 mF capacitor, which are 4.6 times, 2.6 times and 7.4 times the highest reported values, respectively. Further study shows that the ITNG works well under sound in a wide range of sound intensity levels (SILs) and frequencies, and its output is sensitive to the SIL and frequency of the sound, which reveals that the ITNG can act as a self-powered active sensor for real-time noise surveillance and health care. Moreover, this generator can be used to directly power the Fe(OH)₃ sol electrophoresis and shows great potential as a wireless power supply in the electrochemical industry.

Introduction

Harvesting energy from the ambient environment to power various low power-consumption sensors is a fundamental challenge for the internet of things.^{1–10} Sound energy, as one of the most widely distributed energy sources, would provide a potential solution toward this challenge. Though the power density of environmental sound energy is relatively low compared to other energy forms such as solar energy (a plane sonic wave with the sound intensity of 140 dB has a power intensity of 10 mW cm⁻² in air), it is still large enough for powering most nano/micro sensors. Traditionally, most sound energy harvesters are fabricated based on the piezoelectric and

acoustic effects.^{11–15} B. Li *et al.* have used a piezoelectric device containing a straight tube resonator with lead zirconate titanate (PZT) piezoelectric cantilever plates to harvest traveling sound.¹⁶ With an incident sound pressure level (SPL) of 110 dB, an output power density of 0.635 mW m⁻² was obtained. S. B. Horowitz *et al.* have reported a micromachined acoustic energy harvester with a compliant piezoelectric back-plate Helmholtz resonator.¹⁷ They have got an output power density of 0.34 $\mu\text{W cm}^{-2}$ at a SPL of 149 dB. F. Liu *et al.* developed an acoustic energy harvester using an electromechanical Helmholtz resonator with a piezoelectric diaphragm.¹⁸ At a SPL of 160 dB, they obtained an output power density of 9.36 mW m⁻², which can be calculated from its output power of 30 mW and the area of the device. For these piezoelectric sound harvesters, the conversion of acoustic energy to electric energy was achieved *via* piezoelectric transduction in a piezoelectric film and its output performance was enhanced by utilizing the Helmholtz resonator to strengthen the pressure of the incident sound. So the performance of the piezoelectric material and the properties of the resonator jointly determined the output performance of these sound harvesters. For the piezoelectric material, a high d_{33} value and appropriate stiffness to resonate with driven sound are needed to effectively harvest sound energy, but this kind of candidate material is rare and quite difficult to be found at present. And for the resonator, on one hand, it can only strengthen the pressure of the incident sound at certain frequency that makes the incident sound resonate with the resonator as well as the device. At other frequencies, it actually lowers the sound pressure. As a consequence, the frequency bandwidth of the sound that can be harvested is narrowed by the resonator.^{19,20} On the other hand, in order to increase the vibration amplitude at the resonant frequency, the shape and size of the resonant cavity require precise design, which should be done under the guidance of complex calculation.^{21–26} In addition, the whole size of the sound harvesters would be increased by nearly 800 times due to mounting the resonator, such as a 4 cm × 2 cm × 0.7 mm bimorph piezoelectric plate equipped with a 4 cm × 5 cm × 42 cm rectangular straight tube.¹⁶ In such design, the

^aInstitute of Nanoscience and Nanotechnology, School of Physical Science and Technology, Lanzhou University, Lanzhou, 730000, China.
 E-mail: qinyong@lzu.edu.cn

^bThe Research Institute of Biomedical Nanotechnology, Lanzhou University, Lanzhou, 730000, China

†Electronic supplementary information (ESI) available. See DOI: 10.1039/c5nr09087c

‡Authors with equal contribution.

resonator incidentally adds an extra volume for the piezoelectric sound harvester, which takes up much more space and limits the application of sound energy harvesters. So it is still urgently needed to develop some advanced technologies to fabricate a sound harvester with high output and stronger practicability.

The triboelectric nanogenerator (TENG),^{27–34} a newly invented technology based on the principle of coupling between triboelectrification and electrostatic induction,^{35–40} has been intensively studied because of its enormous potential to scavenge mechanical vibration energy and transform it into electricity.^{41–48} J. Yang *et al.* firstly reported a thin-film based TENG to harvest acoustic energy with a Helmholtz cavity.⁴⁹ It generates a short-circuit current of 15.1 μA , an open-circuit voltage of 60.5 V and a maximum output power density of 60.2 mW m^{-2} . Compared with the piezoelectric based sound harvester with a Helmholtz resonator, this TENG based device shows excellent performance in harvesting sound energy. When considering the application of micro/nano electronic devices, the corresponding power sources should not add too much volume or weight. But without the resonator, the output would be 40 times lower than that with the resonator.¹⁶ Therefore, the low output is still a main drawback of sound energy harvesters. N. Y. Cui *et al.* reported a TENG with a sandwich structure composed of two substrates and one vibrating membrane to harvest sound energy without an acoustic resonator.⁵⁰ They have obtained a short-circuit current of 450 μA , an open-circuit voltage of 90 V, and a charging rate of 61 $\mu\text{C s}^{-1}$ for a 1 mF capacitor. This is great progress in independently harvesting sound energy without a resonator. However, this sound energy harvester composed of only one vibrating membrane is not sufficient to fully absorb sound energy due to its limited sound reception area and friction area.

To further improve the performance of the TENG based sound energy harvester without a resonator, we developed a sound driven ITNG with an optimized three-dimensional structure. By integrating more functional layers into an ITNG, we greatly enhanced the short-circuit current to 2.1 mA, the open-circuit voltage to 232 V, and the charging rate to 453 $\mu\text{C s}^{-1}$ for a 1 mF capacitor. To the best of our knowledge, this output is the highest in the current sound energy harvesters. The dependence of the output signals on SIL and frequency is also systematically studied. Furthermore, the ITNG is directly used to power the $\text{Fe}(\text{OH})_3$ sol electrophoresis.

Results and discussion

The ITNG is fabricated by alternatively stacking two kinds of layers named Layer A and Layer B. Fig. 1a shows the structural illustration of the ITNG with three layers. From top to bottom, Layer A is composed of one spacer, one Al-coated porous polyvinyl chloride (PVC) shelf and a layer of polyvinylidene fluoride (PVDF) nanofibers, and Layer B consists of one spacer, one Al layer, one polyethylene (PE) substrate and a layer of PVDF nanofibers. Here both in Layer A and Layer B, the Al layer has

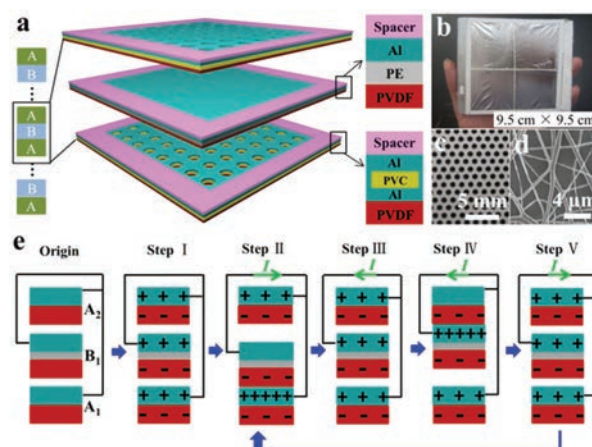


Fig. 1 The schematic and working mechanism of the sound driven ITNG. (a) Structure of the ITNG. (b) Optical image of the ITNG. (c) Optical image of the porous PVC shelf. (d) SEM image of the electrospun PVDF nanofibers. (e) Schematic of the working principle of the sound driven ITNG with 2 units. At Origin stage, no charge is generated; at step I, the charges generated after a certain time of vibration; at step II and V, positive charges flow from Layer B to Layer A; at step III and IV, positive charges flow reversely.

dual functions, one as a frictional layer and the other as an electrode. Fig. 1b is the optical image of the ITNG. In the device, Layer A builds the fundamental structure and Layer B serves as the vibrating membrane. Fig. 1c is the optical image of the porous PVC substrate with deposited Al on its two sides. The array of pores in the shelf with an average diameter of 1 mm allows air circulation, which guarantees sound propagation and reserves more sound energy upon the vibrating membrane. The spacer connects Layer A with Layer B along the four edges and creates a square cavity at the center between them for the vibration of Layer B. As depicted in Fig. 1d, the PVDF nanofibers, with the diameter ranging from 300 nm to 700 nm, act as the frictional surface. The fabrication process in detail is discussed in the Experimental section.

The working mechanism of the ITNG is schematically depicted in Fig. 1e. To simplify the description, the ITNG with three layers is still chosen to represent the device and the PVC substrate in Layer A is omitted here. From the bottom up, the three layers in this sandwich-like structure are marked as A_1 , B_1 , and A_2 , respectively. It can be clearly seen that every adjacent two layers could form a triboelectric generator unit. Thus, there are two triboelectric generator units between the three layers and they are connected in parallel. In the original state, the vibrating membrane B_1 is separated from the shelves A_1 and A_2 , demonstrated as A_1 and A_2 in Fig. 1e, by the spacer (here it is omitted and represented by air of the center cavity) as shown in the “Origin” state. Once the acoustic source is switched on, B_1 begins to vibrate under the sound. Then B_1 frequently rubs with A_1 and A_2 . According to the triboelectric series, electrons are injected from Al into PVDF, resulting in net negative charges on PVDF and net positive charges on Al as shown in Step I. It should be noted that the bound negative triboelectric

charges on PVDF could be retained in PVDF owing to its insulating properties, while the positive charges on the Al electrode are free to move with the change of the electric potential difference (EPD). The EPD between B_1 's electrode and A_1 's electrode is marked as EPD_1 . And the EPD between B_1 's electrode and A_2 's electrode is marked as EPD_2 . When B_1 moves downwards and approaches A_1 as shown in Step II, EPD_1 gradually increases to its peak value, while EPD_2 decreases to the minimum. Both changes lead the free charges on B_1 's electrode to gradually transfer to A_1 's electrode. When B_1 returns to its original position as shown in Step III, EPD_1 begins to decrease and EPD_2 begins to increase, resulting in the reverse flow of free charges. When B_1 keeps moving upwards and approaches A_2 as depicted in Step IV, EPD_1 gradually decreases to its minimum and EPD_2 reaches its peak value, driving free charges to transfer from A_2 's electrode to B_1 's electrode. When B_1 moves downwards, A_1 , B_1 and A_2 recover to their original positions with a reversed charge flow, as shown in Step V. When B_1 keeps moving downwards, A_1 , B_1 , and A_2 return to Step II and a cycle of the electricity generation process is completed. The mechanism shows that the triboelectric charges totally come from the friction between Layer A and Layer B. Adding units indeed adds more frictional surfaces and fully making use of the two sides of each layer further adds more working units between every layer, thus the device will generate more triboelectric charges and increase the total current in the external circuit.

To investigate the reliance of the short-circuit current (I_{sc}) and the open-circuit voltage (V_{oc}) on the number of triboelectric nanogenerator units, six ITNGs with different unit numbers were tested under sound. Here a mini speaker is used as the sound source to produce vibration on the ITNG. At a well-calibrated frequency of 200 Hz and a SIL of 100.5 dB, the I_{sc} and the V_{oc} of ITNGs with different unit numbers are presented in Fig. 2a and b, respectively. The I_{sc} and the V_{oc} exhibit alternating current behavior, which can be clearly seen from Fig. S1a and b.† The output electrical signals are strongly related to the unit number in the ITNG. When the number of units is increased from one to four, the peak value of the output current gradually increases from 0.9 mA to 2.1 mA, then decreases to 1.4 mA when the number of units is increased to six. The maximum current output is 4.6 times the highest reported value.⁵⁰ Divided by the area of the device ($9.5 \text{ cm} \times 9.5 \text{ cm}$), the corresponding current density can reach 232.7 mA m^{-2} and the peak power (I^2R) density at the load resistance of 100Ω is 5414.9 mW m^{-2} , which are 5.2 times and 26.8 times the previous records.⁵⁰ The highest peak value of the output voltage is 232 V generated by the ITNG with one unit and then gradually drops to 137 V when the number of units is increased to six. And the maximum voltage output is 2.6 times as large as the previous one.⁵⁰ The change tendency for the peak value of the output current and the output voltage can be explained as follows. The peak value of the output current is mainly determined by the total charge quantity flowing in the external circuit and the separation speed of the triboelectric surfaces. For the total triboelectric charge

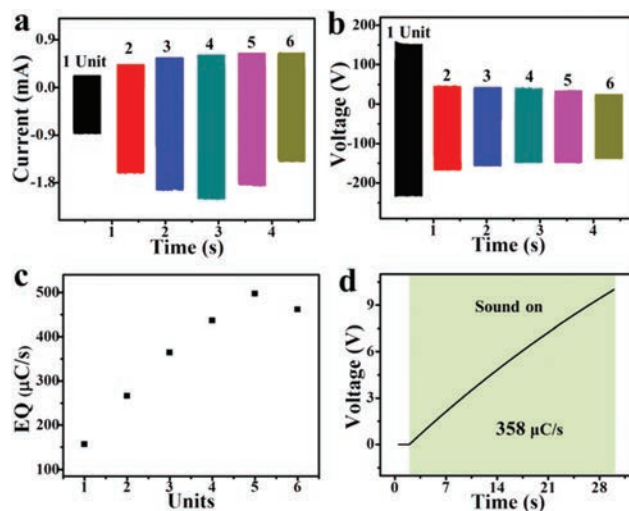


Fig. 2 Electric measurement results of the sound driven ITNG. (a) Short-circuit current and (b) Open-circuit voltage of the ITNGs with different working units driven under a 100.5 dB sound wave at 200 Hz. (c) Charging rates (EQ) of the ITNGs. The charging rate is an average electric quantity in one second calculated from the integral value of the current curves. (d) Voltage curve across a storage capacitor (1 mF) when charged by the ITNG with 5 units at 100.5 dB and 200 Hz rectified by a full-wave rectifying bridge.

quantity, it changes in two aspects when adding one more generator unit. Firstly, one more triboelectric surface represents more triboelectric charge that will be generated for the whole ITNG. And next, one more unit causes a diminishment in the sound pressure for each unit in the ITNG, resulting in a weakened vibration and a reduced triboelectric charge quantity. With the change in the above two aspects, the total triboelectric charge quantity first increases and then decreases when the charge quantity generated by the newly added unit cannot offset the diminished quantity from the former units. At the same time, the separation speed of the vibrating membrane is also slowed down by the diminished sound pressure. Thus, influenced by the total triboelectric charge quantity and the separation speed of the triboelectric surfaces, the output current firstly increases and then decreases with the increasing number of units. Yet the output voltage mainly depends on the charge density on the frictional surface and their distance apart. The separation distance also is reduced by the weakened vibration with more units, but the charge density on the triboelectric surface remains unchanged. As a consequence, the output voltage decreases with addition of the units. The dependence of the charging rate and the unit number is also investigated, in which the charging rate is an average value of the electric quantity in one second. At first, the theoretical calculated charging rate is the integral result of these short-circuit current curves in Fig. 2a. As shown in Fig. 2c, the theoretical calculated charging rate (EQ) first increases to its peak value of $500 \mu\text{C s}^{-1}$ at five units, and finally decreases when the number of units changes from five to six. For the charging rate, it is mainly related to the total quantity of tribo-

electric charges, which we have discussed above. And then, the practical measured charging rate of the five unit ITNG is also studied and shown in Fig. 2d. By connecting the ITNG with a full-wave bridge rectifier, a capacitor of 1 mF is charged continually under sound at the frequency of 200 Hz and the SIL of 100.5 dB to test its practical charging ability. It can be easily seen that the capacitor is charged from 0 V to 10 V within only 28 s and the practical measured charging rate reaches $358 \mu\text{C s}^{-1}$, which is much higher than $61 \mu\text{C s}^{-1}$ reported in our previous work.⁵⁰ Compared with the EQ in Fig. 2c, the practical measured charging rate is a little lower due to the leakage of the capacitor during the charging process. These results confirm that the ITNG shows excellent performance in converting sound energy into electric energy as a good sound energy harvester and its performance can be effectively improved through tactfully integrating more structural units.

As mentioned before, sound in real circumstances has a wide distribution of SIL. To study the effect of the SIL on its output, a five unit ITNG is tested under sound with different SILs under a certain frequency (200 Hz). By adjusting the mini speaker, sound with a series of SILs from 73.0 dB to 102.0 dB can be obtained. As demonstrated in Fig. 3a and b, the I_{sc} and the V_{oc} clearly increase with the increase of the SIL. At a SIL as small as 75.4 dB, the ITNG gives the I_{sc} of 23 μA and V_{oc} of 2 V. When the SIL increases to 100.5 dB, the I_{sc} and the V_{oc} are up to 1.8 mA and 103 V, respectively. Fig. 3c shows the charging curves for a 1 mF capacitor under different SILs at the frequency of 200 Hz. From the charging curves, the practical measured charging rate is calculated and plotted in Fig. 3d. These results indicate that with the increase of the SIL, the charging rate monotonically increases from $7 \mu\text{C s}^{-1}$ to $453 \mu\text{C s}^{-1}$, which is 7.4 times the previous record.⁵⁰ This pheno-

menon can be explained as follows. The increment of the SIL results in stronger vibration with a larger amplitude of Layer B, which could increase the actual friction area and triboelectric charge quantity. Thus the charging rate increases with the increase of SIL. The investigation of the ITNG's properties at different SILs demonstrates that it could be used to efficiently harvest sound energy with different intensities. And the monotonous relationship between the output signals and the SIL shows its potential for real-time sound intensity detection in our daily life.

Besides its different intensities, sound wave has a wide distribution of frequency. To study its frequency response ability, the ITNG is tested under different frequencies. Fixing the SIL at 75.4 dB, the mini speaker is adjusted to provide acoustic waves with a series of frequencies, from 100 Hz to 450 Hz with a step of 25 Hz. The output current and output voltage of the five unit ITNG are depicted in Fig. 4a and b, respectively. In addition, a further enlarged view of the output current and output voltage at the frequency of 275 Hz is shown in Fig. 4c and d respectively, in which the period of the output peak is 3.63 ms. It can be found that the period time accurately

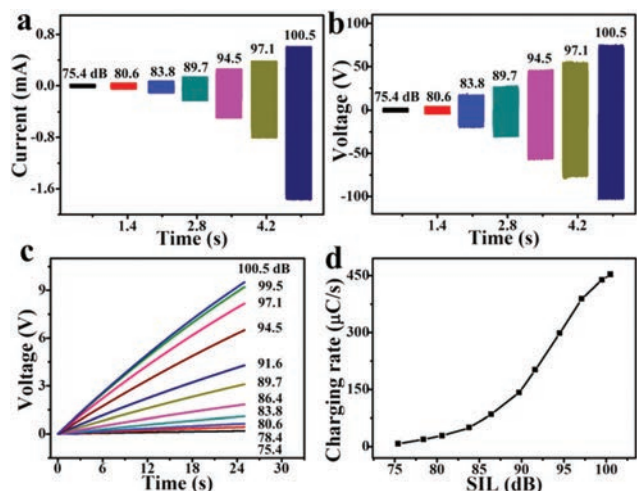


Fig. 3 Output performance of the ITNG with 5 units under sound with a fixed frequency of 200 Hz and different SILs. (a) Short-circuit current. (b) Open-circuit voltage. (c) Different voltage curves across a storage capacitor (1 mF) when charged by the ITNG after rectifying its output signal by a full-wave rectifying bridge under different SILs. (d) The charging rate (average electric quantity in one second stored in the capacitor) for a capacitor under different SILs and 200 Hz constant frequency.

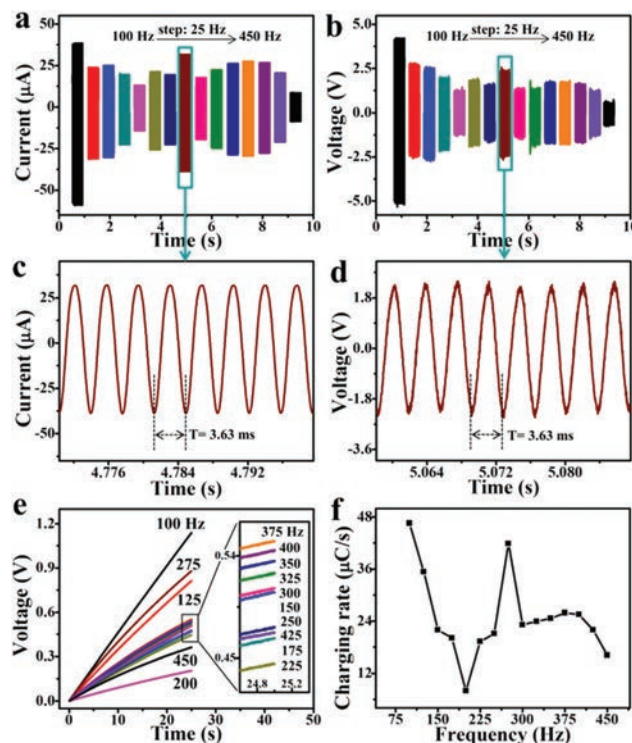


Fig. 4 Output performance of the ITNG with 5 units under sound with 75 dB constant SIL and different frequencies from 100 Hz–450 Hz with a step of 25 Hz. (a) Short-circuit current. (b) Open-circuit voltage. (c) Enlarged view of the short-circuit current. (d) Enlarged view of the open-circuit voltage. (e) Different voltage curves across a storage capacitor (1 mF) when charged by the ITNG after rectifying its output signal by a full-wave rectifying bridge under different frequencies. (f) The charging rate (average electric quantity in one second stored in the capacitor) for a capacitor under different SILs and 75 dB constant SIL.

matches with the driven frequency, which displays the potential of the ITNG to be used as a self-powered sound frequency detector. Then a capacitor (1 mF) is charged by the five unit ITNG driven by sound with different frequencies, which is shown in Fig. 4e. The insert in Fig. 4e shows an enlarged view of a part of the charging curves. Based on these charging curves for the 1 mF capacitor, the practical measured charging rate is calculated and given in Fig. 4f. Driven by different driving frequencies, the ITNG gives a different charging rate. A maximum charging rate reaches $47 \mu\text{C s}^{-1}$ at the frequency of 100 Hz. And at the frequency of 200 Hz, the charging rate reaches the minimum of $8 \mu\text{C s}^{-1}$. This study well demonstrated that the ITNG has the ability to harvest sound energy in a wide frequency range, which shows strong practicability for harvesting different kinds of sound energy.

In consideration of its superior performance in harvesting environmental sound energy, the ITNG is expected to be applied in more aspects even in the electrochemical industry. As a fundamental technique in electrochemical separation and analysis methods, electrophoresis has been widely used in analytical chemistry, biochemistry, pharmacology, clinical chemistry, pharmaceuticals, immunology, microbiology, food chemistry, and other fields. The chemical reaction in the electrochemical process needs to be coupled with the electric field action, for which some sustainable self-sufficient and independent power sources are greatly desired for the development of the electrochemical industry. The ITNG presented above has displayed excellent performance in converting environmental sound energy into electric energy. Therefore, this ITNG has the potential to be used in the electrochemical industry as a power supply when there is sound energy in the surroundings. Here, we successfully demonstrated $\text{Fe}(\text{OH})_3$ sol electrophoresis directly using the ITNG as the power source. The experimental setup is shown in Fig. 5a. The ITNG was placed on a mini speaker and its two output ends were connected to a full-wave rectifying bridge whose two output ends were then connected with the cathode and anode of the $\text{Fe}(\text{OH})_3$ sol in the U-type tube, respectively. The principle for the electrophoresis process is schemed in Fig. 5b and c. The $\text{Fe}(\text{OH})_3$ sol and KNO_3 assistant solution were poured into the U-type tube in sequence. As the cathode and anode, two copper wires were doused in the KNO_3 solution and kept away from the $\text{Fe}(\text{OH})_3$ sol. Before working, there is no change in the U-type tube. And the $\text{Fe}(\text{OH})_3$ sol remains uniform in color, which shows that the colloidal particles are uniformly dispersed. Once the ITNG starts working, the positively charged colloidal particles begin to move to the cathode under the electric field. Fig. 5d and e give the rectified output voltage and current applied on the $\text{Fe}(\text{OH})_3$ sol. In half an hour, the migration state of the colloidal particle is recorded per five minutes as shown in Fig. 5f. With the electrophoresis proceeding, the color near the anode changes from red to colorless and the color near the cathode becomes dark red. This process powerfully demonstrates that this ITNG works effectively in transforming sound energy into electric energy and possesses great potential as a power supply in the electrochemical industry.

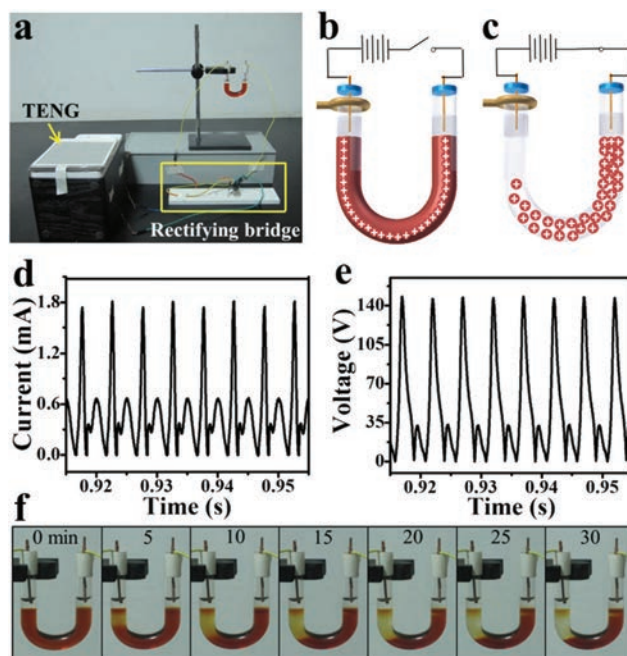


Fig. 5 $\text{Fe}(\text{OH})_3$ sol electrophoresis experiment directly using the sound driven ITNG with 5 units as the power source. (a) Optical image of the experimental setup of the $\text{Fe}(\text{OH})_3$ sol electrophoresis experiment, (b) and (c) are the schematic electrophoresis processes of $\text{Fe}(\text{OH})_3$ colloidal solution when the ITNG is turned on and off, (d) and (e) are separately the rectified short-circuit current and the rectified open-circuit voltage of the ITNG driven by sound with the frequency of 200 Hz and a SIL of 100.5 dB. (f) Optical images of the $\text{Fe}(\text{OH})_3$ sol electrophoresis at different times.

Conclusions

In this work, we demonstrate a new type of integrated triboelectric nanogenerator to harvest ambient sound energy. Driven by sound, it can generate a short-circuit current density up to 232.7 mA m^{-2} and a peak power density up to 5414.9 mW m^{-2} . It is capable of harvesting sound energy in a wide range of SIL and frequency, which displays its potential as a self-powered sound detector. With the virtue of simple fabrication and low cost, the ITNG with a three dimensional integrated structure opens a new way for effectively harvesting sound energy. Moreover, a successful demonstration of directly powering the $\text{Fe}(\text{OH})_3$ sol electrophoresis using the ITNG exhibits a good prospect to be the power supply in the electrochemical industry, which will extend its application to a wide range of fields.

Experimental section

Electrospinning of PVDF nanofiber

First of all, 3.75 g PVDF, 8.5 g *N,N*-dimethylacetamide (DMAC) and 12.75 g acetone are mixed in a 50 ml triangular flask. Then, they are vigorously stirred at $60 \text{ }^\circ\text{C}$ for 30 minutes to form a uniform solution. To begin with electrospinning, the

uniform solution is added into a syringe. And then, the electrospinning is conducted at a high voltage of 15 kV, a feed rate of 3 mL h⁻¹, and a distance between the needle and collector of 16 cm. Finally, the electrospun nanofibers are dried at 60 °C for 3 hours in a ventilated oven. Also the detailed parameters can be seen in our reported work.⁵¹

Fabrication of layer A

At first, a piece of a porous PVC shelf (10 cm × 10 cm × 0.5 mm) is cleaned by drip washing successively with ethanol and deionized water. Then, it is dried by blowing with airgun. After that, a layer of Al (thickness of 100 nm) is deposited on both the sides of the PVC shelf *via* magnetron sputtering. In this way, the deposited Al on both sides is connected and conductive. Finally, by electrospinning, PVDF nanofibers are deposited on one side of the porous PVC shelf above deposited with Al. With above operations, Layer A is fabricated. Here, the Al layer acts both as the frictional layer and the electrode of Layer A. And the PVDF nanofibers act as another frictional layer.

Fabrication of layer B

Firstly, a piece of commercial PE film (10 cm × 10 cm × 5 μm) is tiled on the experimental table and fixed at a quadrature glass shelf along its four edges. Then, a layer of Al (thickness of 100 nm) is deposited on one side of the PE film *via* magnetron sputtering. Finally, PVDF nanofibers are deposited on the other side of the PE film by the electrospinning process. After these operations, Layer B is completed. Here, the Al layer also acts both as one frictional layer and the electrode of Layer B. And the PVDF nanofibers act as another frictional layer.

Fabrication of ITNG

The two sides of Layer A (Layer B) are designed with two different frictional materials, Al and PVDF, thus both of their two sides can work in the ITNG with good integration. Before assembling, the spacer is made by double-sided tape with a thickness of 30 μm. At first, a spacer is glued along the four edges of Layer A on its side without PVDF nanofibers. At the same time, another spacer is glued along the four edges of Layer B on its side without PVDF nanofibers as well. Then, Layer A and Layer B are placed with the spacer facing up. During assembly, one Layer A and one Layer B are alternately added and glued, by which the ITNG with desired layers can be fabricated. As shown in Fig. 1a, in the ITNG, the Al on Layer A faces the PVDF nanofibers on Layer B and separated by the spacer on Layer A, and then the Al on Layer B faces the PVDF nanofibers on Layer A and separated by the spacer on Layer B. From the bottom up, it's in the same order. Here, the spacer is used to create a cavity for the friction during work. And to keep the PE membrane tight and flat, a spacer with the cruciform structure is added on the PVC substrate in Layer A. At the end, all the Al electrodes on Layer A are connected together as one electrode and all the Al electrodes on Layer B are connected together as the other electrode for the subsequent electric performance measurements.

Preparation of Fe(OH)₃ sol electrophoresis

The dark brown Fe(OH)₃ sol is prepared by slowly adding saturated FeCl₃ solution into boiling deionized water and then purified using a dialysis membrane to remove electrolyte ions, like Fe³⁺, Cl⁻. After that, CO(NH₂)₂ is added to the purified Fe(OH)₃ sol to increase the density of the solution, which guarantees the stable existence of hierarchical liquid with KNO₃ solution. KNO₃, as the assistant solution, stays above the Fe(OH)₃ sol to avoid the colloid becoming turbid when the power source is turned on.

Acknowledgements

We sincerely appreciate the support from NSFC (no. 51322203, 51472111, 51302120), the National Program for Support of Top-notch Young Professionals, the Fundamental Research Funds for the Central Universities (no. lzujbky-2014-m02, lzujbky-2015-118, lzujbky-2015-208), PCSIRT (no. IRT1251).

Notes and references

- 1 Y. Q. Zhan, Y. F. Mei and L. R. Zheng, *J. Mater. Chem. C*, 2014, **2**, 1220–1232.
- 2 C. B. Williams, C. Shearwood, M. A. Harradine, P. H. Mellor, T. S. Birch and R. B. Yates, *IET Circ. Devices Syst.*, 2001, **148**, 337–342.
- 3 Z. L. Wang and J. H. Song, *Science*, 2006, **312**, 242–246.
- 4 B. Z. Tian, X. Zheng, T. J. Kempa, Y. Fang, N. Yu, G. Yu, J. Huang and C. M. Lieber, *Nature*, 2007, **449**, 885–889.
- 5 Y. Qin, X. D. Wang and Z. L. Wang, *Nature*, 2008, **451**, 809–813.
- 6 R. S. Yang, Y. Qin, L. Dai and Z. L. Wang, *Nat. Nanotechnol.*, 2008, **4**, 34–39.
- 7 K. Y. Lai, G. J. Lin, Y. L. Lai, Y. F. Chen and J. H. He, *Appl. Phys. Lett.*, 2010, **96**, 081103.
- 8 Y. Yang, K. C. Pradel, Q. S. Jing, J. M. Wu, F. Zhang, Y. S. Zhou, Y. Zhang and Z. L. Wang, *ACS Nano*, 2012, **6**, 6984–6989.
- 9 Y. Yang, S. H. Wang, Y. Zhang and Z. L. Wang, *Nano Lett.*, 2012, **12**, 6408–6413.
- 10 S. Bai, L. Zhang, Q. Xu, Y. B. Zheng, Y. Qin and Z. L. Wang, *Nano Energy*, 2013, **2**, 749–753.
- 11 S. N. Cha, J. S. Seo, S. M. Kim, H. J. Kim, Y. J. Park, S. W. Kim and J. M. Kim, *Adv. Mater.*, 2010, **22**, 4726–4730.
- 12 S. Cha, S. M. Kim, H. Kim, J. Ku, J. I. Sohn, Y. J. Park, B. G. Song, M. H. Jung, E. K. Lee, B. L. Choi, J. J. Park, Z. L. Wang, J. M. Kim and K. Kim, *Nano Lett.*, 2011, **11**, 5142–5147.
- 13 M. Carrara, M. R. Cacan, M. J. Leamy, M. Ruzzene and A. Erturk, *Appl. Phys. Lett.*, 2012, **100**, 204105.
- 14 H. Y. Lee and B. Choi, *Smart Mater. Struct.*, 2013, **22**, 115025.
- 15 S. Noh, H. Lee and B. Choi, *Int. J. Precis. Eng. Manuf.*, 2013, **14**, 1629–1635.

- 16 B. Li, J. H. You and Y. J. Kim, *Smart Mater. Struct.*, 2013, **22**, 055013.
- 17 S. B. Horowitz, M. Sheplak, L. N. Cattafesta and T. Nishida, *J. Micromech. Microeng.*, 2006, **16**, S174–S181.
- 18 F. Liu, A. Phipps, S. Horowitz, K. Ngo, L. Cattafesta, T. Nishida and M. Sheplak, *J. Acoust. Soc. Am.*, 2008, **123**, 1983–1990.
- 19 S. K. Tang, *J. Sound Vib.*, 2005, **279**, 1085–1096.
- 20 D. Li and L. Cheng, *J. Sound Vib.*, 2007, **305**, 272–288.
- 21 J. M. De. Bedout, M. A. Franchek, R. J. Bernhard and L. Mongeau, *J. Sound Vib.*, 1996, **202**, 109–123.
- 22 G. T. Lei, R. W. Techentin and B. K. Gilbert, *IEEE Trans. Microwave Theory Tech.*, 1999, **47**, 562–569.
- 23 A. Selamet, N. S. Dickey and J. M. Novak, *J. Sound Vib.*, 1995, **187**, 358–367.
- 24 N. S. Dickey and A. Selamet, *J. Sound Vib.*, 1996, **195**, 512–517.
- 25 R. C. Chanaud, *J. Sound Vib.*, 1997, **204**, 829–834.
- 26 A. Selamet, I. J. Lee and N. T. Huff, *J. Sound Vib.*, 2003, **262**, 509–527.
- 27 F. R. Fan, L. Lin, G. Zhu, W. Wu, R. Zhang and Z. L. Wang, *Nano Lett.*, 2012, **12**, 3109–3114.
- 28 F. R. Fan, Z. Q. Tian and Z. L. Wang, *Nano Energy*, 2012, **1**, 328–334.
- 29 G. Zhu, C. Pan, W. Guo, C. Y. Chen, Y. Zhou, R. Yu and Z. L. Wang, *Nano Lett.*, 2012, **12**, 4960–4965.
- 30 V. Nguyen and R. S. Yang, *Nano Energy*, 2013, **2**, 604–608.
- 31 Z. L. Wang, *Faraday Discuss.*, 2014, **176**, 447–458.
- 32 G. Zhu, P. Bai, J. Chen, Q. S. Jing and Z. L. Wang, *Nano Energy*, 2015, **14**, 126–138.
- 33 Z. L. Wang, J. Chen and L. Lin, *Energy Environ. Sci.*, 2015, **8**, 2250–2282.
- 34 Z. Wang, L. Cheng, Y. B. Zheng, Y. Qin and Z. L. Wang, *Nano Energy*, 2014, **10**, 37–43.
- 35 J. G. Kirkwood and F. H. Westheimer, *J. Chem. Phys.*, 1938, **6**, 506.
- 36 K. S. Pitzer, *J. Solution Chem.*, 1975, **4**, 249–265.
- 37 S. E. Feller, R. W. Pastor, A. Rojnuckarin and S. Bogusz, *J. Phys. Chem.*, 1996, **100**, 17011–17020.
- 38 G. S. P. Castle, *J. Electrostat.*, 1997, **40**, 13–20.
- 39 L. S. McCarty and G. M. Whitesides, *Angew. Chem., Int. Ed.*, 2008, **47**, 2188–2207.
- 40 H. T. Baytekin, A. Z. Patashinski, M. Branicki, B. Baytekin, S. Soh and B. A. Grzybowski, *Science*, 2011, **333**, 308–312.
- 41 J. Chen, G. Zhu, W. Yang, Q. Jing, P. Bai, Y. Yang, T. C. Hou and Z. L. Wang, *Adv. Mater.*, 2013, **25**, 6094–6099.
- 42 W. Q. Yang, J. Chen, G. Zhu, J. Yang, P. Bai, Y. J. Su, Q. S. Jing, X. Cao and Z. L. Wang, *ACS Nano*, 2013, **7**, 11317–11324.
- 43 W. Yang, J. Chen, G. Zhu, X. Wen, P. Bai, Y. Su, Y. Lin and Z. L. Wang, *Nano Res.*, 2013, **6**, 880–886.
- 44 J. Yang, J. Chen, Y. Yang, H. Zhang, W. Yang, P. Bai, Y. Su and Z. L. Wang, *Adv. Energy Mater.*, 2014, **4**, 1301322.
- 45 W. Yang, J. Chen, Q. Jing, J. Yang, X. Wen, Y. Su, G. Zhu, P. Bai and Z. L. Wang, *Adv. Funct. Mater.*, 2014, **24**, 4090–4096.
- 46 H. Zhang, Y. Yang, Y. Su, J. Chen, K. Adams, S. Lee, C. Hu and Z. L. Wang, *Adv. Funct. Mater.*, 2014, **24**, 1401–1407.
- 47 X. Fan, J. Chen, J. Yang, P. Bai, Z. L. Li and Z. L. Wang, *ACS Nano*, 2015, **9**, 4236–4243.
- 48 J. Yang, J. Chen, Y. J. Su, Q. S. Jing, Z. L. Li, F. Yi, X. N. Wen, Z. N. Wang and Z. L. Wang, *Adv. Mater.*, 2015, **27**, 1316–1326.
- 49 J. Yang, J. Chen, Y. Liu, W. Q. Yang, Y. J. Su and Z. L. Wang, *ACS Nano*, 2014, **8**, 2649–2657.
- 50 N. Y. Cui, L. Gu, J. M. Liu, S. Bai and Y. Qin, *Nano Energy*, 2014, **15**, 321–328.
- 51 Y. B. Zheng, L. Cheng, M. M. Yuan, Z. Wang, L. Zhang, Y. Qin and T. Jing, *Nanoscale*, 2014, **6**, 7842–7846.